The Astrophysical Journal, 694:205–213, 2009 March 20 doi:10.1088/0004-637X/694/1/205

ANISOTROPIC WINDS FROM CLOSE-IN EXTRASOLAR PLANETS

James M. Stone[1] and Daniel Proga[2]
[1] Department of Astrophysical Sciences, Princeton University, Princeton, NJ 08544, USA
[2] Department of Physics, University of Nevada, Las Vegas, NV 89154, USA
Received 2008 September 12; accepted 2008 December 18; published 2009 March 13

ABSTRACT

We present two-dimensional hydrodynamic models of thermally driven winds from highly irradiated, close-in extrasolar planets. We adopt a very simple treatment of the radiative heating processes at the base of the wind, and instead focus on the differences between the properties of outflows in multidimensions in comparison to spherically symmetric models computed with the same methods. For hot ($T \gtrsim 2 \times 10^4$ K) or highly ionized gas, we find that strong (supersonic) polar flows are formed above the planet surface which produce weak shocks and outflow on the night side. In comparison to a spherically symmetric wind with the same parameters, the sonic surface on the day side is much closer to the planet surface in multidimensions, and the total mass-loss rate is reduced by almost a factor of 4. We also compute the steady-state structure of interacting planetary and stellar winds. Both winds end in a termination shock, with a parabolic contact discontinuity which is draped over the planet separating the two shocked winds. The planetary wind termination shock and the sonic surface in the wind are well separated, so that the mass-loss rate from the planet is essentially unaffected. However, the confinement of the planetary wind to the small volume bounded by the contact discontinuity greatly enhances the column density close to the planet, which might be important for the interpretation of observations of absorption lines formed by gas surrounding transiting planets.

Key words: hydrodynamics – methods: numerical – planetary systems – stars: winds – outflows

Online-only material: color figures

1. INTRODUCTION

A significant fraction (about 20%) of extrasolar giant planets (EGPs) discovered to date have an orbit with a semimajor axis of less than 0.1 AU (Schneider 2008). For such close-in EGPs, heating of the upper layers of the atmosphere by irradiation from the central star, especially in the extreme ultraviolet (EUV), can produce an extended envelope of gas, and perhaps even drive a wind (e.g., Moutou et al. 2001; see Ehrenreich 2008 for a review). Direct detection of an extended envelope surrounding HD209458b has been reported (Vidal-Madjar et al. 2003, 2008; Ehrenreich et al. 2008), based on the absorption of stellar Lyα during transits. The fraction of the stellar Lyα flux absorbed by HD209458b is so large that it must be surrounded by a cloud of neutral hydrogen that extends beyond the Roche lobe of the planet, and therefore is unbound (although see Ben-Jaffel 2007 for an alternative analysis of the same observations). The observations also place a lower limit on the mass-loss rate from the planet of $\dot{M} \gtrsim 10^{10}$ g s^{-1}, although the actual rate could be much higher since the absorption is saturated.

Detailed theoretical models of winds from highly irradiated EGPs are of interest not only to interpret the observations but also to place firmer constraints on the mass-loss rates. If these rates are a factor of few hundred times higher than the lower limit observed in HD209458b, then over its lifetime the planet will lose a significant enough fraction of its total mass to alter its structure and evolution (Hubbard et al. 2007; Lecavelier des Etangs 2007).

A useful measure of the strength of the wind expected from a highly irradiated EGP is the ratio of gravitational potential to thermal energy at the top of the atmosphere, usually termed the hydrodynamic escape parameter, that is,

$$\lambda = \frac{GM_p\mu}{R_p kT}, \qquad (1)$$

where M_p and R_p are the mass and radius of the planet, and T and μ are the temperature and mean mass per particle in the atmosphere. For $\lambda \gg 1$, the atmosphere is tightly bound and a hydrodynamic wind is not expected, although a weak outflow may still be produced by a variety of nonthermal processes, e.g., Hunten (1982). For $\lambda \lesssim 10$, a thermally driven hydrodynamic (Parker) wind will be produced (for reference, $\lambda \approx 15$ for 10^6 K plasma in the solar corona at $2R_\odot$). When evaluated at the effective temperature $T_{\rm eff} \approx 10^3$ K of HD209458b, $\lambda \approx 140$, indicating that a hydrodynamic wind is unlikely. However, it has been pointed out that the upper layers of close-in EGPs will be heated to $T \sim 10^4$ K by the intense EUV radiation from the central star (Lammer et al. 2003; Yelle 2004; see Ballester et al. 2007 for possible observational detection of this hot gas). At this temperature, and if the gas is mostly neutral, $\lambda \approx 14$ (a value similar to that in the solar corona) so that a thermally driven wind is possible. On the other hand, if the gas is ionized (reducing μ), or if the temperature is slightly higher (both of which are relevant for EGPs around young stellar objects (YSOs) or higher-mass stars), then λ can be even smaller.

Calculating the structure and mass-loss rate from a thermally driven hydrodynamic wind from close-in EGPs requires solving the time-dependent equations of hydrodynamics, with a proper accounting of the radiative heating at the base of the wind. The latter is probably the most challenging aspect of the problem, and different approaches have led to different estimates of the mass-loss rates. To simplify the calculation, all of the models presented to date are one dimensional (spherically symmetric). Watson et al. (1981) presented models for the escape of hydrogen from the terrestrial planets in the early solar system, using a simplified treatment of the heating that deposits all of energy in a single zone at the base of the wind. Scaled-up versions of these models have been applied to EGPs. Tian et al (2005) improved these solutions by using a multidimensional radiative transfer calculation to estimate the radial distribution of the heating rate

(the underlying hydrodynamic models are still one dimensional, however). Lecavelier des Etangs et al. (2004) pointed out that tidal forces could distort the gravitational potential isosurfaces around the planet, and this could affect the mass-loss rate (Erkaev et al. 2007), but only if the shape and location of the sonic surface are significantly altered. Yelle (2004) has presented more realistic models of the wind from close-in EGPs including chemistry, photoionization and recombination, and thermal and molecular diffusion in a hydrodynamic model (again assuming spherical symmetry). New models with a similar level of sophistication have recently been computed for HD209458b by García Muñoz (2007), and for EGPs in general by Murray-Clay et al. (2008).

As has been pointed out by many authors, the fact that close-in EGPs are irradiated on only one side calls into question the assumption of spherical symmetry. The problem is exasperated by the fact that close-in EGPs will be tidally locked, so that the only mechanisms that can transport heat to the night side are bulk flows in the atmosphere and thermal conduction. Although global circulation models are beginning to be investigated for close-in EGPs (e.g., Dobbs-Dixon & Lin 2008; Showman et al. 2008), these models do not apply to the weakly bound hot ($T \sim 10^4$ K) gas in the upper atmosphere. For HD209458b, the advection time for gas moving at the sound speed to move halfway around the planet is ≈11 hr, much longer than the radiative cooling time for the hot gas. Thus, there is likely to be a large contrast in the temperature between the day and night sides in the upper layers of the atmosphere which serve as the base of the wind, even if the temperature at the infrared photosphere is more uniform. The amplitude of this contrast is, however, uncertain.

The goal of this paper is to investigate the effect that anisotropic heating has on the winds from close-in EGPs using two-dimensional numerical hydrodynamic calculations. Given the uncertainties in the mass-loss rate produced by different treatments of the radiative heating and microphysics in the wind, we adopt the simplest possible approach, and focus on the relative difference between our multidimensional calculations and spherically symmetric models computed with identical techniques. We find there are important differences in multidimensions. For example, the sonic surface in the wind is moved much closer to the planet, and the overall mass-loss rate is reduced by almost a factor of four for a nearly isothermal wind. Our numerical approach also allows us to consider the interaction between planetary and stellar winds. Although a stellar wind does not affect the mass-loss rate, it confines the planetary wind to a small volume and greatly enhances the column density close to the planet. These results suggest that incorporating multidimensional effects may be as important as improved treatments of the radiative transfer and microphysics in order to interpret the observations of transiting planets such as HD209458b.

In addition to a simplified treatment of the thermodynamics, we have made a number of other simplifying assumptions in this first investigation. For example, our calculations are two dimensional (axisymmetric), which precludes us from studying the effect of Coriolis forces (orbital motion) on the outflow. Therefore, our models are appropriate only for the flow close to the planet. Fully three-dimensional hydrodynamic models of an *isotropic* wind from orbiting planet have recently been presented by Schneiter et al. (2007). Such calculations are challenging, even with an adaptive mesh these authors could only afford three grid points per planetary radius in the model. In additions, our models are hydrodynamic rather than MHD, even though at large radii the wind may be significantly ionized, and interact with a primarily MHD stellar wind. Finally, there are a number of kinetic plasma effects (e.g., charge-exchange reactions between the planetary and stellar wind particles) that might become important as the wind becomes very diffuse at large radii. These effects are known to be important in the MHD of the heliopause (e.g., Borovikov et al. 2008). Fully three-dimensional MHD models of anisotropic winds from planets including multidimensional radiative transfer, microphysics, and the appropriate kinetic plasma effects are an interesting and important direction for future work.

This paper is organized as follows. In the next section, we describe our numerical methods. In Section 3, we present results for anisotropic winds from isolated EGPs. In Section 4, we consider the interaction of anisotropic winds from an EGP with a stellar wind. Finally, in Section 5 we discuss our results, and in Section 6 conclude.

2. METHOD

We use the time-dependent hydrodynamics code ZEUS (Stone & Norman 1992) to compute the multidimensional structure of an EGP wind. We start our calculations from an initially spherically symmetric outflow, and run them for many crossing times, until the solution has settled into a steady state. Typically this takes less than an hour on a modern workstation. This technique is much simpler than solving the steady-state equations directly, even in one dimensional, because the steady-state ODEs define a two-point boundary value problem which contains a critical point that requires special treatment when solved using shooting or relaxation methods.

We solve the hydrodynamic equations in spherical polar (r, θ) coordinates, that is

$$\frac{\partial \rho}{\partial t} + \frac{1}{r^2}\frac{\partial (r^2 \rho v_r)}{\partial r} + \frac{1}{r \sin\theta}\frac{\partial (\rho v_\theta \sin\theta)}{\partial \theta} = 0 \tag{2}$$

$$\rho\left(\frac{\partial v_r}{\partial t} + v_r\frac{\partial v_r}{\partial r} + \frac{v_\theta}{r}\frac{\partial v_r}{\partial \theta} - \frac{v_\theta^2}{r}\right) = -\frac{\partial P}{\partial r} - \frac{GM_p}{r^2} \tag{3}$$

$$\rho\left(\frac{\partial v_\theta}{\partial t} + v_r\frac{\partial v_\theta}{\partial r} + \frac{v_\theta}{r}\frac{\partial v_\theta}{\partial \theta} + \frac{v_r v_\theta}{r}\right) = -\frac{1}{r}\frac{\partial P}{\partial \theta} \tag{4}$$

$$\frac{\partial e}{\partial t} + v_r\frac{\partial e}{\partial r} + \frac{v_\theta}{r}\frac{\partial e}{\partial \theta} = -\frac{P}{\rho}\left(\frac{1}{r^2}\frac{\partial (r^2 v_r)}{\partial r} + \frac{1}{r\sin\theta}\frac{\partial (v_\theta \sin\theta)}{\partial \theta}\right), \tag{5}$$

where ρ is the mass density, $v_r$and v_θ are the radial and angular components of the velocity, and e is the internal energy density. The pressure P is related to e through the equation of state, $P = (\gamma - 1)e$, which implies $T = (\gamma - 1)\mu e/k\rho$. We also add an artificial viscous stress term to the momentum and energy equations to ensure proper shock capturing, see Stone & Norman (1992) for the details of these terms in spherical polar coordinates. The axis of symmetry of the grid is orientated along the line connecting the centers of the planet and the central star, with $\theta = 0$ the direction towards the star (noon), and $\theta = \pi$ the direction away from the star (midnight).

Although we are solving the dynamical equations in a frame corotating with the planet, we have neglected the Coriolis force terms in Equations (3) and (4). Since we find that the terminal velocity V_∞ of the wind is less than the orbital velocity $V_{\rm orb}$ of an EGP at 0.1 AU from a solar type star (typically, we find

$v_\infty \sim V_{\rm esc} < V_{\rm orb}$ where $V_{\rm esc} \approx 40\,{\rm km\,s^{-1}}$ is the escape velocity from the planet), then the neglect of Coriolis forces limits the applicability of our solutions to regions close to the EGP. On larger scales (on order of the orbital radius), the planetary wind will be deflected by Coriolis forces, and swept back by the stellar wind into a cometary shape (Moutou et al. 2001; Vidal-Madjar et al. 2003). We discuss physical effects that are likely to be important for the structure of the wind on large scales in Section 5.

Also note that we do not explicitly include heating, cooling, or thermal conduction terms in the energy Equation (5). Instead of injecting a fixed rate of heating at the base of the wind, and then modeling the cooling and conduction processes that determine the temperature, we simply fix the temperature directly. Operationally, in the first grid cell above the lower boundary condition at the surface of the planet $r = R_p$, we hold the density at a constant ρ_0, and set the internal energy to

$$e(R_p, \theta) = e_0 \max(0.01, \cos\theta), \tag{6}$$

where $e_0 = \rho_0/[\gamma(\gamma-1)]\lambda_0$. This introduces the hydrodynamic escape parameter at the base of the wind λ_0 as a free parameter. By holding $\rho = \rho_0$ and $e = e_0$ in the first radial cell, the wind solution emerges naturally from the density and pressure gradients above this cell. Provided that the acceleration region between this cell and the sonic point is well resolved, the flow (including the mass-loss rate) is then set self-consistently by the resulting density and pressure gradients. This technique is identical to procedure we have used before to model radiative driven winds in a disk geometry (e.g., Proga et al. 1998, 2000). Typically we have at least 20 cells in the wind acceleration region below the sonic point. The angular distribution we have assumed for the internal energy (Equation (6)) gives a temperature ratio of 100 between the day and night sides. Since the amplitude of this ratio is uncertain, we will also present results in the following section for a model in which this ratio is only two.

We have also computed models in which the both the internal energy and density are varied according to Equation (6), so that the temperature at the base of the wind is fixed (this may be a better model of a photoionized atmosphere, where higher UV fluxes on the day side produce ionization at higher densities, but produce little change in the temperature). Since the pressure distribution in the wind using this method is identical to simply varying e, we find essentially no change between models launched with fixed temperature or fixed density at the base.

Equations (2)–(5) are discretized on a grid of 200 radial and 200 angular cells, in the domain $1 \leqslant r/R_p \leqslant 50$ and $0 \leqslant \theta \leqslant \pi$. We use a nonuniform grid in the radial direction, with the size of each successive radial cell increased by the ratio $\delta r_{i+1}/\delta r_i = 1.02$. This gives better resolution in the inner regions of the grid (at $r = R_p$, $\delta r/R_p \approx 0.02$), and also keeps the cells nearly square throughout the domain ($r\delta\theta \approx \delta r$). The boundary conditions at $\theta = 0$ and π are given by symmetry conditions. At the outer radial edge of the grid, we use outflow boundary conditions (all variables projected at zero slope). At the inner radial edge, we use a reflecting boundary condition.

We initialize the grid above the first radial cell to contain extremely low density ($\rho = 10^{-20}\rho_0$) gas within an internal energy profile $e(r, \theta) = e_0/r^2$, a uniform outward radial velocity $v_r = C_s$, where $C_s^2 = \gamma(\gamma-1)e_0/\rho_0 = 1/\lambda_0$, and no angular motion $v_\theta = 0$. The outward flow helps to prevent gravitational infall developing in the outer regions, and the low density helps to reduce transients. The flow crossing time across the entire grid is $t \sim L/C_s = 50$, where L is the radius of the outer boundary. We find by $t \approx 100$, a steady solution has been established. All of the results presented in this paper are at a time of $t = 200$. We have confirmed that the steady state wind solution is independent of how we initialize the wind, and is converged with the numerical resolution used here (quantities such as the mass-loss rate and terminal velocity change by less than 1% if the numerical resolution is halved in each direction).

The primary parameters that determines the wind solution are the adiabatic index γ and λ_0 at the base of the wind. We discuss wind solutions for a variety of values for γ, from $\gamma = 1.01$ (nearly isothermal) to $\gamma = 5/3$ (adiabatic). We use $\lambda_0 = 5$ for most of the models presented in this study, which implies $\lambda = 500$ on the night side. The value $\lambda_0 = 5$ is three times smaller than the value for HD209458b, assuming the gas temperature is $T = 10^4$ K, and that it is mostly neutral. Choosing a smaller value of λ_0 is mostly a numerical convenience: higher values lead to much lower density winds in which transients are much more severe, and therefore take much longer to reach a steady state. In fact, the value $\lambda_0 = 5$ is relevant to EGP winds which are ionized (and therefore have smaller λ for the same temperature), or in which the temperature is slightly (a factor of two) larger. Both cases are relevant to EGPs around YSOs with higher UV fluxes, or which orbit higher-mass central stars. In order to investigate the structure of winds with higher λ_0, we will also present a model with $\lambda_0 = 10$.

To test our numerical methods, and to compare with previous models, we have calculated a number of spherically symmetrical models with different values of λ_0 and γ. Our method reproduces the location of the sonic point in one-dimensional Parker winds (Keppens & Goedbloed 1999) to better than 1%. We have also recovered the same structure and mass-loss rates for isothermal winds found by Watson et al. (1981) and Tian et al. (2005) for both $\lambda = 5$ and 15.

3. RESULTS

We start by discussing the two-dimensional structure of a nearly isothermal wind, $\gamma = 1.01$, with $\lambda_0 = 5$. Figure 1 shows images of the density (with velocity vectors overlaid) and temperature in the inner regions $r/R_p \leqslant 10$ after the flow has relaxed to a steady state. Remarkably, even though $\lambda = 500$ on the night side of the planet, far too large to drive an appreciable wind, the density in the outflow near $\theta = \pi$ is quite large. This indicates that there must be a substantial nonradial flow around the planet to maintain a significant density on the night side. Contours of the density are slightly elongated in the polar directions compared to the region near $\theta = \pi/2$, by about a factor of 5/4, indicating that the density in the wind is mildly anisotropic.

A prominent feature in the density is a discontinuity that starts at $\theta \approx 3\pi/4$ near the planet, and curves to smaller angles as it extends outward in radius. This feature is a shock front produced by the geometrical compression of the wind as it flows from the day side to the night side of the planet, and is further indication of strong nonradial motions in the outflow. The polar flow can be seen more clearly in the pattern of velocity vectors. Close to the planet (at $r \leqslant 2\,R_p$), the velocity in the wind near the region near $\theta = \pi/2$ is nearly purely polar, while on the night side there is *inflow* rather than outflow. At large radii, there is a nearly perfectly radial outflow at all angles, although the length of the velocity vectors clearly shows that the terminal velocity is larger on the day side in comparison to the night side. We investigate the velocity field of the wind more thoroughly below.

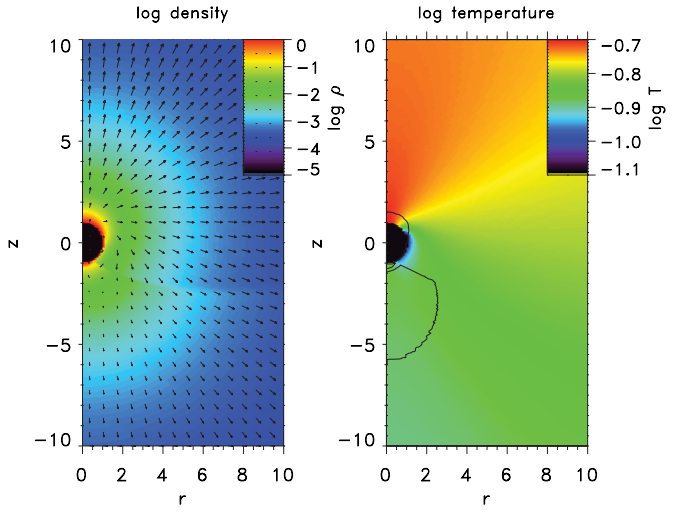

Figure 1. Left: density (in units of ρ_0, the value at the base of the wind) and velocity vectors (in units of the Keplerian velocity at R_p) in a nearly isothermal ($\gamma = 1.01$) thermally driven wind from a close-in EGP irradiated on one side only. Right: temperature, in units of $GM_p\mu/(kR_p)$, for the same calculation. The solid line in the temperature plot shows the sonic surfaces. The irradiating star is located toward the top (corresponding to $\theta = 0$).

(A color version of this figure is available in the online journal.)

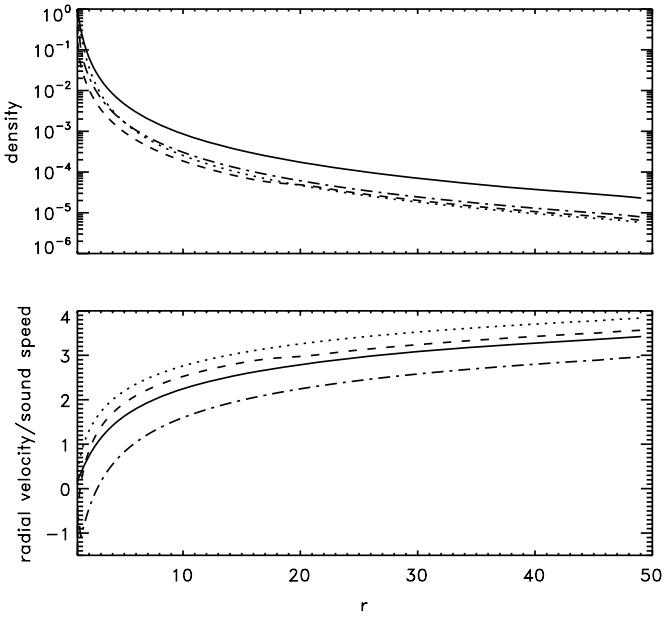

Figure 2. Radial profiles of the density and radial velocity (normalized by the sound speed) at $\theta = 0$ (dotted line), $\pi/2$(dashed line), and π (dot-dashed line) for the solution shown in Figure 1. The star is located at $\theta = 0$. The solid line in each panel shows the profile for a spherically symmetric wind with $\lambda_0 = 5$. The radius is measured in units of R_p.

Since for $\gamma = 1.01$ the wind is nearly isothermal, the temperature is not significantly affected by geometrical compression or expansion. The temperature in the wind essentially becomes a passive scalar which is frozen-in to the value set at the surface of the planet, and contours of the temperature are very nearly equal to the streamlines in the flow. Thus, the temperature image in Figure 1 demonstrates how the outflow curves around the planet's surface. The temperature in the nightside flow is everywhere constant and equal to the temperature at the base of the wind emanating from $\theta \approx \pi/4$ on the day side, about $\log T \approx -0.85$ in the units used in the figure. There is a small region of lower temperature very close to the planet near the terminator, but at $\theta > 3\pi/4$, the temperature is once again equal to the value elsewhere on the night side, $\log T \approx -0.85$. This is an indication of infall on the night side.

Overlaid on the temperature image are contours of the sonic surface, i.e., regions where $|v|/C_s = 1$, where v is the total magnitude of the velocity, including both the radial and polar components. On the day side, the sonic surface is located at about $0.5\,R_p$ above the surface of the planet, and this decreases to zero at the terminator, as expected. The contours on the night side of the planet indicate a region where the wind is *decelerated* to subsonic flow by the shock front identified in the density image. The flow is then re-accelerated to supersonic outflow at $r \gtrsim 5\,R_p$ (for $\theta = \pi$). The contour very near the surface of the planet on the night side indicates supersonic infall there. For comparison, the sonic surface for a spherically symmetric wind with $\lambda_0 = 5$ is located at roughly $1.5\,R_p$ above the surface of the planet. Thus, the sonic surface is moved substantially closer to the surface of the planet in the anisotropic case.

Figure 2 shows radial slices of the density and radial Mach number, v_r/C_s, at $\theta = 0$, $\pi/2$, and π. Also shown for comparison is the spherically symmetric wind for the same value of λ_0. The difference in the density in the outflow between the day side and the night side is large only very close to the planet; near $r = 2\,R_p$ the density on the day side can be nearly an order of magnitude larger than on the night side. This difference drops to less than a factor of 2 at $10\,R_p$, and becomes even smaller farther out. However, the density at all angles is much less than the spherically symmetric case, by a factor of close to 4. The radial Mach number shows that the flow speed is faster than the spherical case on the day side, about the same at the terminator, and significantly slower on the night side. Infall on the night side is clearly evident by the negative values for the Mach number below $r/R_p \approx 3$. An important quantity is the mass-loss rate in the wind. For this model, we find that the total (angle-integrated) steady-state mass-loss rate is a factor of 3.7 smaller than the spherically symmetric case.

The nonradial flow in the wind can be explored by one-dimensional slices in polar angle at different radii. Figure 3 shows slices of the density and both components of the velocity (scaled to the sound speed) taken at $r/R_p = 2$, 5, 10, and 50. The amplitude of the spherically symmetric solution at these locations is also shown for each quantity. The shock front evident in the density image (Figure 1) is most prominent in the polar velocity (bottom panel of Figure 3). At small radii, there is a large increase in the polar velocity moving from the day to night sides, until there is a sudden, discontinuous drop at $\theta \approx 3\pi/4$. This trend is repeated in each slice at larger radii, except the maximum amplitude of the polar velocity drops, and the shock front is moved to smaller angles. At $r/R_p = 2$, the polar velocity is supersonic, reaching a maximum Mach number of about 1.5. The location of the shock is also clearly evident in the angular profiles of the density. At each radius there is a slow decrease in the density moving from the day side to the night side, with a discontinuous jump at the location of the shock front. The shock is weak, it produces a density jump of only about 2.5 at $r/R_p = 2$. The radial velocity is not strongly affected by the shock, a reflection of the fact that this component of the velocity is almost parallel to the nearly radial shock front. Instead, the primary feature of the radial velocity is a systematic decrease from the day side to the night side.

To explore the effect of varying γ on the two-dimensional structure of the wind, Figure 4 shows images of the density

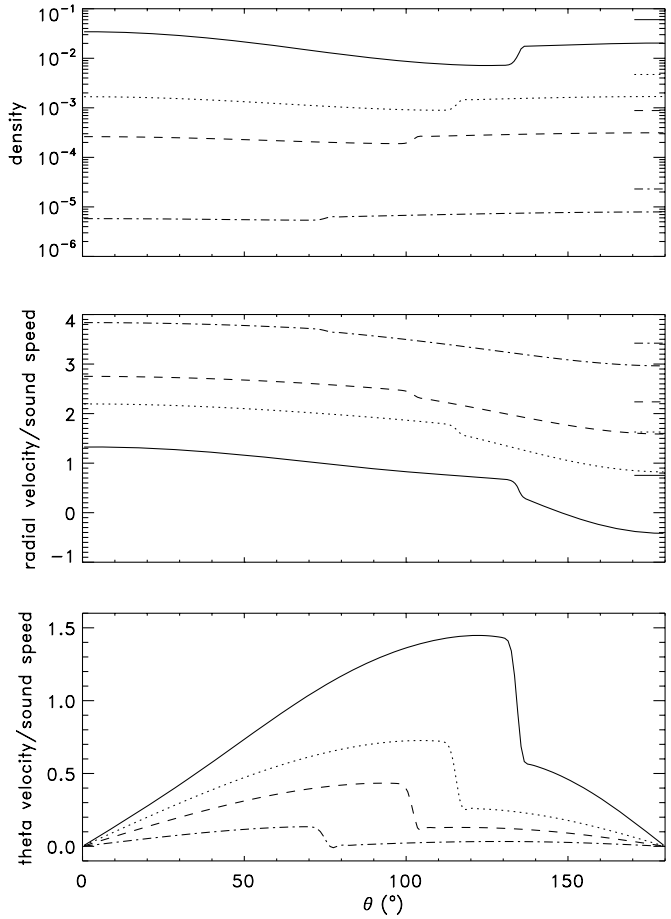

Figure 3. Angular profiles of the density, radial and angular velocity (both scaled by the sound speed) at $r/R_p = 2$ (solid line), 5 (dotted line), 10 (dashed line), and 50 (dot-dashed line). The horizontal tick marks at the right edge of the top two plots show the amplitude of the spherical wind solution with $\lambda_0 = 5$ at the same radial locations.

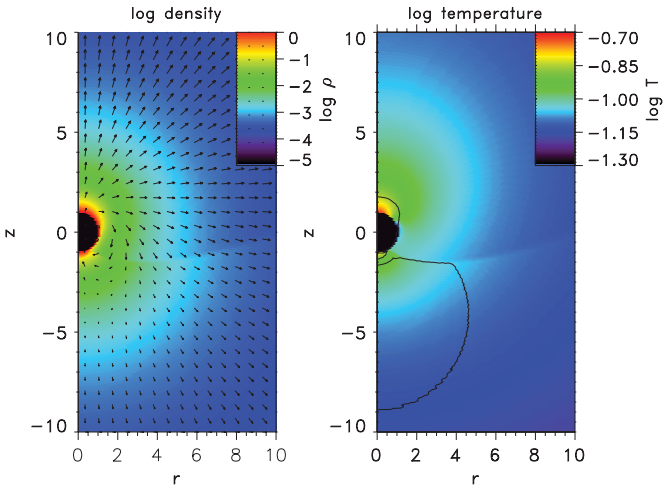

Figure 4. Left: density (in units of ρ_0, the value at the base of the wind) and velocity vectors (scaled to the Keplerian velocity at R_0) for a anisotropic EGP wind with $\gamma = 1.1$. Right: temperature, in units of $GM_p\mu/(kR_p)$, for the same calculation. The solid line in the temperature plot shows the sonic surfaces. The irradiating star is located toward the top.

(A color version of this figure is available in the online journal.)

and temperature (with velocity vectors and the sonic surface overlaid) from a model computed using $\gamma = 1.1$, but otherwise identical to the nearly isothermal model discussed above. Comparison of Figures 1 and 4 show that the density structure of the wind is very similar in the two cases. The polar flow toward the night side of the planet is very clear in the pattern of the velocity vectors in Figure 4. Once again, the length of the vectors demonstrates that the outflow velocity is much higher on the day side in comparison to the night side. The temperature profile in the wind for $\gamma = 1.1$, however, is quite different than that for $\gamma = 1.01$. Now, adiabatic expansion produces significant cooling in the wind, so the temperature at large radii drops dramatically. Moreover, the shock which decelerates the polar flow toward the night side produces a significant jump in temperature, and so is clearly visible in the right panel of Figure 4. Due to the slower acceleration of the wind, the sonic surface is moved to larger radii, it is now at about 0.8 R_p above the surface of the planet. This is still much smaller than the spherically symmetric case, where for $\gamma = 1.1$ the sonic surface is about 3 R_p above the planet surface. The mass-loss rate in this case is about 2.9 times smaller than the mass rate in a spherically symmetric wind with the same λ_0 and γ, and this value is 2 times smaller than the mass-loss rate in the anisotropic wind with $\gamma = 1.01$ discussed above.

As γ is increased further, the general structures noted above remain the same, however, the outflow becomes systematically weaker. For γ close to 5/3, a thermally driven wind is not possible, and we find no steady-state outflow (Keppens & Goedbloed 1999).

We have also computed a model in which the minimum internal energy on the night side in Equation (6) is $0.5e_0$, giving a temperature ratio of two between the day and night sides. We use $\gamma = 1.01$ and $\lambda_0 = 5$ to allow direct comparison to the model discussed above. As expected, the flow in this case is more nearly spherically symmetric. However, important features such as the location of the sonic surface are little changed from the result shown in Figure 1, so that the total mass-loss rate is nearly identical to the model with a larger temperature contrast. Since the details of the wind depend on the temperature contrast between the day and night sides, determining this ratio at the base of the wind (as opposed to the infrared photosphere) from observations is important.

Finally, we have also explored the effect of increasing λ_0 on the properties of the wind. Figure 5 presents radial slices of the density and radial Mach number, v_r/C_s, at $\theta = 0$, $\pi/2$, and π. Also shown for comparison is the spherically symmetric wind for the same value of λ_0. The density at all angles is much smaller (more than an order of magnitude) than the $\lambda_0 = 5$ case presented in Figure 2. As before, the difference in the density in the outflow between the day side and the night side is not large. Moreover, the density at all angles is not significantly different than the spherically symmetric case, it is only a factor of 0.8 smaller. Thus, for this large value of λ_0, anisotropic effects are reduced. The plot of the radial Mach number indicates the reason why: the sonic surface of the wind is moved to much larger radii, about 3 R_p. Two-dimensional images of the flow show that the density below the sonic surface is nearly spherically symmetric. There is a very strong, nearly supersonic polar flow below the sonic surface that transports heat and mass to the night side. The region below the sonic surface forms an extended atmosphere which serves as the base of a nearly spherically symmetric wind. While the difference in the flow pattern in this case is of interest, it may not be realistic due to the simplified treatment of the thermodynamics. The polar circulation (which is analogous to the flow in a general circulation model) that produces a spherical

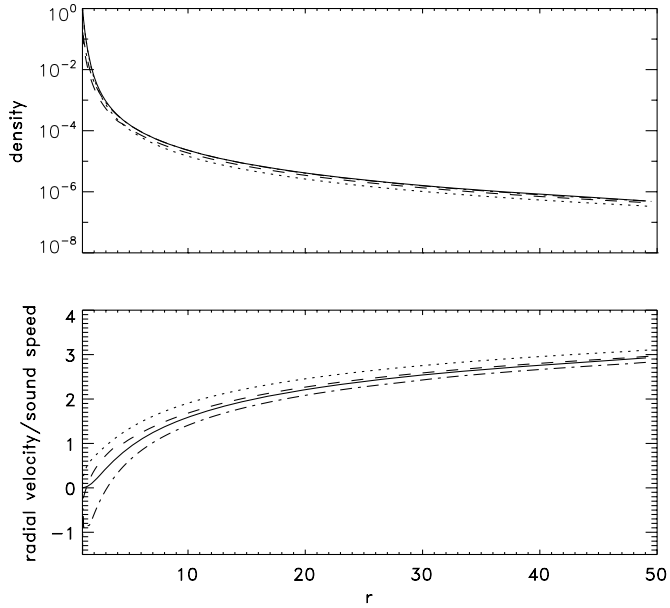

Figure 5. Radial profiles of the density and radial velocity (normalized by the sound speed) at $\theta = 0$ (dotted line), $\pi/2$(dashed line), and π (dot-dashed line) for a model with $\lambda_0 = 10$. The star is located at $\theta = 0$. The solid line in each panel shows the profile for a spherically symmetric wind with the same λ_0. Radius is measured in units of R_p.

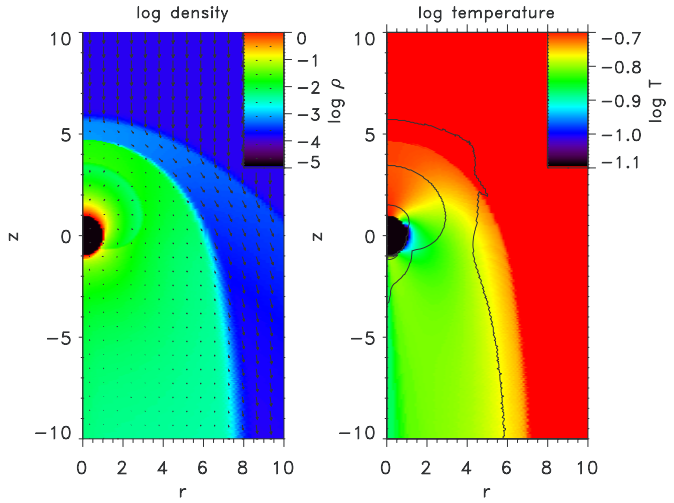

Figure 6. Left: density (in units of ρ_0, the value at the base of the wind) and velocity vectors (scaled to the Keplerian velocity at P_0) for an anisotropic EGP wind with $\gamma = 1.01$ interacting with a uniform stellar wind. Right: temperature in units of $GM_p\mu/(kR_p)$, for the same calculation. The solid line in the temperature plot shows the sonic surfaces. The star is located toward the top.

(A color version of this figure is available in the online journal.)

wind is likely strongly affected by the local heating and cooling processes, which we have not modeled directly here. Thus, we conclude that the structure of EGP winds in multidimensions can be affected by the value of λ_0 at the base of the wind, and that models with large values of λ_0 require more realistic treatments of radiative heating and cooling. Since larger values of λ_0 are likely relevant to many observed EGPs, exploring this regime with more realistic multidimensional models is important.

4. THE INTERACTION OF PLANET AND STELLAR WINDS

Using the numerical methods adopted for this study, it is straightforward to compute the interaction of an anisotropic wind from a close-in EGP with the wind from the central star. As an initial condition, we use the steady-state structure of the fiducial wind model (with $\gamma = 1.01$) studied in the previous section, computed using $\lambda_0 = 5$. We restart this model with the outer boundary condition modified to represent an inflowing stellar wind. Specifically, for $\theta \leqslant \pi/2$, we set the density and internal energy at the outer boundary to be constants, ρ_* and e_*, respectively, and set the radial and angular velocities to be $v_r = v_* \cos\theta$ and $v_\theta = v_* \sin\theta$, where $\rho_* = 10^{-4}\rho_0$, $e_* = 2.5 \times 10^{-3} e_0$, and $v_*/C_{s,*} = -\sqrt{5}$, where $C_{s,*}$ is the sound speed in the stellar wind. We then follow the propagation of the stellar wind across the grid, and stop the calculation when the structure resulting from its interaction with the anisotropic EGP wind has settled into a steady state.

Note that for the parameter values adopted for the stellar wind, $C^2_{s,*}/C^2_{s,0} = 25$, that is the stellar wind is much hotter than the planet wind. For the properties of HD209458b, the stellar wind would have a velocity of $\approx$90 km s^{-1} and a temperature of 2.5×10^5 K, both within the range of stellar wind properties expected for EGPs (Preusse et al. 2005). Note also that pressure-driven stellar winds do not reach their terminal velocity until many stellar radii, so that a planet with an orbital radius of $\lesssim$0.1 AU may still be inside the wind acceleration region. Furthermore, the stellar wind is likely to be magnetized, so that the interaction between the two should be MHD. Finally, since the stellar wind velocity is comparable to the orbital velocity of the planet, in the frame of reference of the planet (in which our computations are performed), the stellar wind would arrive from a direction offset by a large angle from the line connecting the centers of the star and planet. Thus, the interaction should ideally be computed in full three-dimensional MHD; however, this is beyond the scope of this study. Three-dimensional hydrodynamic models of the interaction of planet and stellar winds have been presented by Schneiter et al. (2007).

Figure 6 shows images of the density (with velocity vectors overlaid) and temperature after the interacting planetary and stellar winds have settled into a steady state. The density image shows that the planetary wind is swept back into a parabolic-shaped region that opens toward the night side of the planet. This region is bounded by a contact discontinuity that separates the shocked planet and stellar winds. A shock in the stellar wind upstream of this contact is clearly visible as a discontinuity in the density. The pattern of velocity vectors shows how this shock diverts the stellar wind around the region occupied by the outflow from the planet. A shock in the planet wind upstream of the contact discontinuity is also clearly visible in the density image at r/R_p of between 3 and 3.5 for $0 \leqslant \theta \leqslant \pi/2$. At large radii the density in the planetary wind is remarkably constant with radius. This is because the cross-sectional area of the parabolic region occupied by the planet wind is nearly constant at large radii, so that there is no further geometrical expansion in the planetary wind. Thus, once the planetary wind reaches terminal velocity, its density becomes constant.

The temperature image again mostly shows streamlines in the flow, since the model is nearly isothermal. In contrast to the flow shown in Figure 1, the flow in Figure 6 clearly follows streamlines that strongly curve away from the star in the wind interaction region. Contours of the sonic surface are overlaid on the temperature image in Figure 6. Moving outward from the planet on the day side, there are three contours. The first is the location of the sonic surface in the planetary wind, it is located

about 0.5 R_p above the planet surface. The location and shape of this surface is essentially identical to the case with no stellar wind (Figure 1). The next contour, located at about 2.5 R_p at $\theta = 0$, is the planetary wind termination shock. This contour is identical to the shape of the shock visible in the density image. Clearly, the termination shock *decelerates* the planetary wind to subsonic velocities. Finally, the last contour at about 4.75 R_p above the planet surface at $\theta = 0$, is the stellar wind termination shock. Note that this contour only follows the location of the stellar wind shock visible in the density for angles $\theta \lesssim \pi/4$. This indicates that the transverse velocity becomes supersonic as the stellar wind is diverted around the planet.

It is important to note that the planetary wind sonic surface and the planetary wind termination shock are well separated, by about 2 R_p, over most of the flow. Thus the sonic surface in the planetary wind is little changed by the interaction with the stellar wind; and the stellar wind has little effect on the mass-loss rate from the planet. Of course, the exact location of the wind termination shocks and the contact discontinuity separating the two depends on the assumed momentum flux in the stellar wind. More powerful winds would confine the planetary wind to a region closer to the planet. However, since the momentum flux density in the planet wind increases rapidly near the planet, it would be difficult for the stellar wind to reach the sonic surface of the planetary wind, unless the hydrodynamic escape parameter λ_0 was considerably larger.

The radial profiles of the density at angles of $\theta = \pi/2$ (terminator) and π (away from star) are shown in Figure 7. For comparison, the profile for a spherically symmetric wind with $\lambda_0 = 5$ is plotted as a solid line. The profile of the density at the terminator (shown as a dashed line) is dominated by a series of steps representing the shocks in the planet and stellar winds, and the contact discontinuity that separates them. Moving outward from the planet, the density decreases sharply in the wind acceleration region, then increases discontinuously at the wind termination shock at $r/R_p \approx 2$. It then drops discontinuously at the contact discontinuity between the shocked winds at $r/R_p \approx 6$, and drops again discontinuously at the stellar wind shock at $r/R_p \approx 10$. Beyond this radius the density is constant, as this region is filled with unshocked stellar wind. In contrast, the slice along the night side (shown as a dot-dashed line) does not cross the boundary between the planet and stellar winds. Thus, in this case the density drops smoothly from the planet surface outward, reaching a constant value by $r/R_p \approx 10$. This is in stark contrast to the density profile in the wind from an isolated planet (see Figure 2), which declines at all radii. At $r/R_p = 10$, the density in this case is over 10 times larger compared to an anisotropic wind with no stellar wind interaction; at $r/R_p = 50$ it is nearly 1000 times larger. Despite this difference, the mass-loss rate in the planetary wind is nearly identical to the case with no stellar wind, because the conditions in the planetary wind at the sonic surface are relatively unaffected. However, the increased density in the planet wind strongly affects the observed column density through the wind, as we discuss in the next section.

5. DISCUSSION

Perhaps the most direct observable of winds from close-in EGPs is the column density of gas surrounding the planet observed during transits. It is of interest to investigate whether the column density of anisotropic winds, and anisotropic winds that are confined by the interaction with a stellar wind, are significantly different from spherically symmetric models.

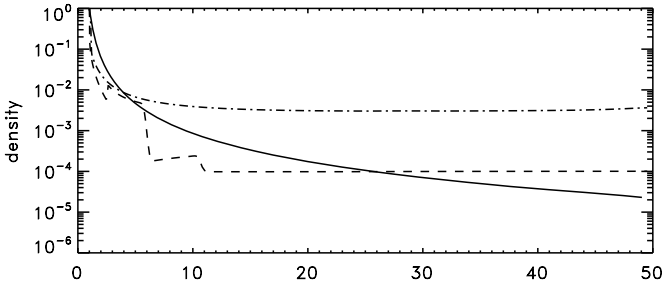

Figure 7. Radial profiles of the density at $\theta = \pi/2$ (dashed line), and π (dot-dashed line) for a planetary wind interacting with a stellar wind. The solid line shows the profile in a spherically symmetric wind. The radius is measured in units of R_p.

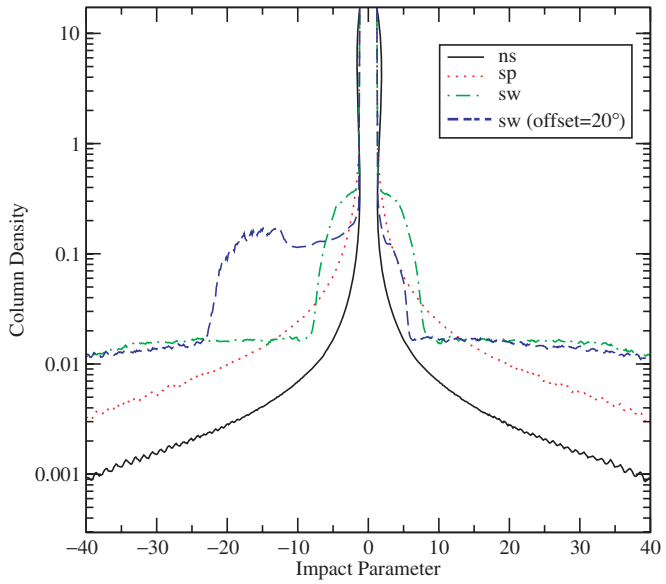

Figure 8. Column density (in arbitrary units) as a function of impact parameter (in units of R_p) for four different models of thermally driven hydrodynamic winds from a close-in EGP. The dotted line (labeled "sp") corresponds to a spherically symmetric wind. The solid line (labeled "ns") corresponds to an anisotropic planetary wind that does not interact with a stellar wind. The dot-dashed line (labeled "sw") corresponds to an anisotropic wind interacting with a stellar wind, with the observer located at an angle of $\theta = \pi$. The dashed line is the same as "sw," but with the observer located at an angle offset by 20° from $\theta = \pi$.

(A color version of this figure is available in the online journal.)

Figure 8 shows profiles of the column density (in arbitrary units) as a function of impact parameter for a spherical EGP wind, an anisotropic EGP wind, and an anisotropic wind that interacts with a stellar wind as viewed from two different angles. With no stellar wind, the comparison of the spherical and anisotropic winds shows that the lower mass-loss rate and density at large radii in the latter significantly reduces the column density at a few planetary radii. However, the situation is reversed as soon as the interaction with a stellar wind is considered. If the observer is located at $\theta = \pi$ (that is, the viewing angle is directly toward the night side), then the column density is strongly enhanced out to the radius of the contact discontinuity between the planetary and stellar winds, because all of the planet wind material is confined to this region. If the interacting winds are viewed at an angle of 20° from $\theta = \pi$, then the region of large column density associated with the compressed planetary wind is extended to one side of the planet, and would be visible as a cometary tail extending away from the planet.

These results suggest that the interaction with a stellar wind can greatly enhance the column density of close-in EGP winds. However, there are some limitations to our results. For $r/R_p \gtrsim 10$, the structure of the planetary wind will be strongly affected by orbital motion and tidal forces from the central star. This will strongly affect the column density at these radii, which warrants further three-dimensional hydrodynamic (Schneiter et al. 2007) and MHD investigations. Moreover, we find that the terminal velocity of an anisotropic planetary wind is only 3–4 C_s, which for 10^4 K gas is only about $V_\infty \approx 30\,\mathrm{km\,s^{-1}}$. This is much smaller than the escape velocity from a solar-type star at 0.1 AU. Thus, although the wind is unbound from the planet, it will not escape the stellar gravitational potential, and will most likely collect in a torus of gas at the orbital distance of the planet. Whether the stellar wind, or radiation pressure, or nonthermal effects such as charge exchange reactions with stellar wind particles, can drive this gas to further radii is uncertain. However, understanding the dynamics of the diffuse gas at large radii could be important for interpreting absorption line studies of transiting systems.

6. CONCLUSIONS

We have presented two-dimensional, hydrodynamic calculations of the steady-state structure of thermally driven winds from highly irradiated, close-in EGPs, including the interaction with a high-velocity wind from the central star. Our primary conclusions are the following.

1. The mass-loss rate in an anisotropic wind is reduced by about a factor of 4 in a nearly isothermal wind ($\gamma = 1.01$) compared to a spherical wind with the same parameters.
2. The sonic point in an anisotropic wind on the day side is located 2–3 times closer to the planet surface compared to a spherically symmetric wind with the same parameters.
3. A supersonic polar flow from the day side to the night side is generated just above the planet surface (within $r/R_p \approx 2$). This flow generates weak shocks due to geometrical compression on the night side. At large radial distances, the outflow is nearly spherically symmetric.
4. The interaction with a stellar wind strongly compresses the planet wind and greatly enhances the column density of the gas in the outflow surrounding the planet. However, the termination shock in the planetary wind is located well above the sonic surface, so the overall mass-loss rate is affected very little.

There are a number of limitations to our results. Probably the most important is the very simplistic treatment of the thermodynamics in the wind that we have adopted in our computations. Rather than attempting to model the heating, cooling, and thermal conduction processes in the wind directly, we have simply fixed the temperature at the base of the wind consistent with previous more detailed models, and computed polytropic models with different γ. However, by comparing our models to spherically symmetric solutions computed using the same techniques and parameters, we are able to isolate the effects that multidimensional dynamics have on the wind. We conclude that these effects can be important, and therefore it is desirable to include a more realistic treatment of the radiative transfer and microphysics (e.g., Murray-Clay et al. 2008) in multidimensional models in the future.

Our conclusions are mostly applicable to winds in which the hydrodynamic escape parameter $\lambda_0 = 5$, a value which is 3 times smaller than that inferred for observed systems such as HD209458b (assuming the temperature at the base of the wind is $T = 10^4$ K, and the wind is mostly neutral). A slightly higher temperature, or an ionized wind would produce a value closer to that adopted in most of our models. For larger values of λ_0, we find that the sonic point is located much farther from the planet, and polar flows produce a spherically symmetric, extended atmosphere above the planet which serves as the base of a nearly spherically symmetric wind. However, the assumptions we have adopted for the thermodynamics in the wind are likely not applicable in this case. Thus, the study of the multidimensional structure of winds in this parameter regime will require more sophisticated treatments of the radiative heating and cooling.

Additional limitations to our calculations are that we have not included the orbital motion of the planet, or the gravitational field of the central star. We also have not included the effects of magnetic fields that are likely to be important in the dynamics of the stellar wind. Finally, nonthermal plasma processes (such as charge exchange reactions) might be important in the extremely low density wind material far from the planet, and since the terminal velocity of the planet winds studied here is less than the orbital velocity of the planet, these processes might even dominate the escape of gas from the system. These limitations suggest that fully three-dimensional MHD models of anisotropic winds from EGPs are warranted, and that ideally these models would span the entire orbital plane of the planet, include possibly important kinetic plasma effects, and would be based on an improved treatment of the thermodynamics in the wind.

We thank the late Bohdan Paczynski, who was an inspiration for the work presented in this paper. We also thank R. Kurosawa for making Figure 8, and A. Burrows, R. Murray-Clay, and R. Rafikov for helpful comments on an early draft. D.P. acknowledges support by the National Aeronautics and Space Administration under grant/Cooperative Agreement No. NNX08AE57A issued by the Nevada NASA EPSCoR program. J.S. thanks the IAS for support as a summer visitor.

REFERENCES

Ballester, G. E., Sing, D. K., & Herbert, F. 2007, Nature, 445, 511
Ben-Jaffel, L. 2007, ApJ, 671, L61
Borovikov, S. N., Pogorelov, N. V., Zank, G. P., & Kryukov, I. A. 2008, ApJ, 682, 1404
Dobbs-Dixon, I., & Lin, D. N. C. 2008, ApJ, 673, 513
Ehrenreich, D. 2008, arXiv:0807.1885v1
Ehrenreich, D., et al. 2008, A&A, 483, 933
Erkaev, N. V., et al. 2007, A&A, 472, 329
García Muñoz, A. 2007, Planet. Space Sci., 55, 1426
Hubbard, W. B., Hattori, M. F., Burrows, A., Hubeny, I., & Sudarsky, D. 2007, Icarus, 187, 358
Hunten, D. M. 1982, Planet. Space Sci., 30, 773
Keppens, R., & Goedbloed, J. P. 1999, A&A, 343, 251
Lammer, H., Selsis, F., Ribas, I., Guinan, E. F., Bauer, S. J., & Weiss, W. W. 2003, ApJ, 598, L121
Lecavelier des Etangs, A. 2007, A&A, 461, 1185
Lecavelier des Etangs, A., Vidal-Madjar, A., McConnell, J. C., & Hébrard, G. 2004, A&A, 418, L1
Moutou, C., et al. 2001, A&A, 371, 260
Murray-Clay, R., Chiang, E., & Murray, N. 2008, ApJ in press (arXiv:0811.0006)
Preusse, S., Kopp, A., Büchner, J., & Motschmann, U. 2005, A&A, 434, 1191
Proga, D., Stone, J. M., & Drew, J. E. 1998, MNRAS, 295, 595
Proga, D., Stone, J. M., & Kalman, T. R. 2000, ApJ, 543, 686
Schneider, J. 2008, The Extrasolar Planets Encyclopedia http://exoplanets.eu

Schneiter, E. M., Velázquez, P. F., Esquivel, A., & Raga, A. C. 2007, ApJ, 671, L57
Showman, A. P., Cooper, C. S., Fortney, J. J., & Marley, M. S. 2008, ApJ, 682, 559
Stone, J. M., & Norman, M. L. 1992, ApJS, 80, 753
Tian, F., Toon, O. B., Pavlov, A. A., & De Sterck, H. 2005, ApJ, 621, 1049
Vidal-Madjar, A., et al. 2003, Nature, 422, 143
Vidal-Madjar, A., et al. 2008, ApJ, 676, L57
Watson, A. J., Donahue, T. M., & Walker, J. C. G. 1981, Icarus, 48, 150
Yelle, R. V. 2004, Icarus, 170, 167, (Icarus, 183, 508, Corrigendum)